Journal of Computational Physics 229 (2010) 1181–1197

Contents lists available at ScienceDirect

Journal of Computational Physics

journal homepage: www.elsevier.com/locate/jcp

One way domain decomposition method with second order transmission conditions for solving electromagnetic wave problems

Zhen Peng *, Vineet Rawat, Jin-Fa Lee

ElectroScience Laboratory, The Ohio State University, 1320 Kinnear Road, Columbus, OH 43212, USA

ARTICLE INFO

Article history:
Received 23 June 2009
Received in revised form 8 October 2009
Accepted 12 October 2009
Available online 27 October 2009

Keywords:
Domain decomposition methods
Second order transmission conditions
Maxwell's equations

ABSTRACT

Non-overlapping domain decomposition (DD) methods with complex first order Robin-type transmission conditions (TCs) provide an efficient iterative solution for Maxwell's equation. Unfortunately, the first order TCs do not effectively account for some eigenmodes of the system matrix, which limits the scalability of the methods. In this work, we examine two TCs with a second order transverse derivative to improve the method's performance. A detailed convergence analysis of the two TCs is presented. We then investigate the use of the two second order TCs in non-conformal and non-overlapping one way DD methods. Numerical results illustrate the effectiveness of the proposed methods on some model problems and on several problems of practical interest.

1. Introduction

Finite Element based domain decomposition (DD) methods have recently garnered considerable attention due to their ability to accurately and efficiently solve large and multi-scale electromagnetic radiation and scattering problems [1–9]. The methods are attractive because they allow the solution of large problems with only modest computational resources. They are also inherently parallel, an important consideration in keeping with current trends in computer architecture. In general, the DD methods derive their efficiency by decomposing the original large FEM problem into several smaller, more manageable sub-domains. The sub-domains are solved individually and adjacent sub-domains are then coupled to one another via transmission conditions (TCs). An iterative process is used to adjust boundary conditions for sub-domain problems until the solution converges to that of the original global problem. The TCs not only enforce the continuity of tangential fields on the interfaces between sub-domains, but they are also directly related to the convergence of DD method.

For the vector wave equation, the majority of non-overlapping DD methods employ complex first order Robin-type transmission conditions (FOTCs) [10–13]. The FOTCs provide a simple, efficient, and parallel preconditioner for the DD matrix equation that yields fast and robust iterative solution. The eigenmodes of the DD operator can be classified as either propagating or evanescent, and the FOTC is effective only for the propagating eigenmodes. This limits the scalability of the DD methods and one must turn to higher order TCs to further improve the performance. As with higher order absorbing boundary conditions [14], a full second order TC (SOTC) is difficult to implement due to a surface divergence term. Instead, we may add a single second order transverse derivative operator to the FOTC. In [15], an interface condition involving a second order tangential operator is introduced. In [16–18], another family of SOTCs are proposed, which damp both propagating and evanescent modes. We refer this family of SOTCs as optimized SOTC (SOTC–OPT). In this work, we also investigate a new type of SOTC, which is shown to improve the eigenspectrum of the DD operator by shifting eigenvalues corresponding to transverse electric (TE) evanescent modes away from the origin. We denote the new TC by second order TC TE, or SOTC–TE.

* Corresponding author. Tel.: +1 614 302 8896.
E-mail addresses: peng.98@osu.edu (Z. Peng), rawat.4@osu.edu (V. Rawat), lee.1863@osu.edu (J.-F. Lee).

0021-9991/$ - see front matter © 2009 Elsevier Inc. All rights reserved.
doi:10.1016/j.jcp.2009.10.024

Herein, we investigate non-conformal, non-overlapping DD methods with the use of the SOTC–OPT and SOTC–TE at subdomain interfaces. In Section 2.1, the problem statement is presented and the decomposed boundary value problem (BVP) used in the DD method is presented in Section 2.2. In Section 2.3, we discuss the convergence analysis of the SOTCs. The weak formulation and discrete formulation for the non-conformal DD methods with SOTCs are discussed in Sections 2.4 and 2.5. In Section 3.1, we examine eigenvalue distribution of the DD matrix using the SOTCs. In Section 3.2, we characterize the new methods by examining their scalability with respect to certain parameters and compare the performance of the new methods to that with FOTC. Lastly, we illustrate the effectiveness of the new methods on a microstrip photonic-bandgap structure (PBG) in Section 3.3. A summary and conclusion are included in Section 4.

2. Formulation

We first introduce some notations and definitions that will be employed throughout this work. Boldface letters (e.g. $\mathbf{u}$) are used to denote vectors in $\mathbb{R}^3$ while an overhead hat (e.g. $\hat{\mathbf{u}}$) will signify that the vector has unit magnitude. Finite dimensional matrices will be represented by uppercase italic characters (e.g. A), while lowercase italic characters will be used to represent column vectors (e.g. x). The imaginary unit will be represented by j. We denote the time-harmonic electric and magnetic fields by E and H, respectively. The free space wave number will be denoted by $k_0 = \omega\sqrt{\mu_0\varepsilon_0}$, where $\omega = 2\pi f$ is the radial frequency of operation and ε_0 and μ_0 are the permittivity and permeability in free space, respectively. The free space intrinsic impedance is given by $\eta_0 = \sqrt{\mu_0/\varepsilon}$. In a material region, the wave number is given by $k = \omega\sqrt{\mu\varepsilon}$ where ε and μ are the permittivity and permeability of the material. Also, we define $\varepsilon_r = \varepsilon/\varepsilon_0$ and $\mu_r = \mu/\mu_0$ as the relative permittivity and permeability of the material.

2.1. Problem statement

In this paper, we are interested in solving large scale electromagnetic problem by using one way domain decomposition methods to clearly demonstrate the performances of various TCs considered in this work. Fig. 1 shows a sample example of one way dissection decomposition of large problem. We replace the unbounded domain $\mathbb{R}^3$ by a bounded domain Ω, with first order absorbing boundary conditions (ABC) imposed on the finite truncation boundary. Subsequently, the mathematical model can be described by:

$$\nabla \times \mu_r^{-1}\nabla \times \mathbf{E} - k_0^2\varepsilon_r\mathbf{E} = -jk_0\eta_0\mathbf{J}^{imp} \quad \text{in } \Omega \tag{1}$$

$$\hat{\mathbf{n}} \times (\mathbf{E} \times \hat{\mathbf{n}}) = 0 \quad \text{on } \Gamma_{\text{PEC}} \tag{2}$$

$$\hat{\mathbf{n}} \times (\mu_r^{-1}\nabla \times \mathbf{E}) = 0 \quad \text{on } \Gamma_{\text{PMC}} \tag{3}$$

$$\hat{\mathbf{n}} \times (\mu_r^{-1}\nabla \times \mathbf{E}) - jk_0\sqrt{\frac{\varepsilon_r}{\mu_r}}\hat{\mathbf{n}} \times (\mathbf{E} \times \hat{\mathbf{n}}) = \hat{\mathbf{n}} \times (\mu_r^{-1}\nabla \times \mathbf{E}^{\text{inc}}) - jk_0\sqrt{\frac{\varepsilon_r}{\mu_r}}\hat{\mathbf{n}} \times (\mathbf{E}^{\text{inc}} \times \hat{\mathbf{n}}) \quad \text{on } \Gamma_{\text{ABC}} \tag{4}$$

Note that the perfect magnetic conductors (PMC) and perfect electric conductors (PEC) are denoted by Γ_{PEC} and Γ_{PMC}, respectively. DD methods are suitable for the solution of this class of problems because they can take advantage of repeated subblocks (see Fig. 1) and provide an efficient and effective preconditioner for the indefinite matrix equation arising from the FE methods.

2.2. Domain decomposition boundary value problem

To simplify the analysis, we will consider a domain $\Omega \subset \mathbb{R}^3$ and its decomposition into $N_p = 2$ sub-domains such that $\Omega = \Omega_1 \cup \Omega_2$ (see Fig. 2). Further, we define the interface between sub-domains as $\Gamma := \partial\Omega_1 \cap \partial\Omega_2$, and the exterior boundaries as $\widetilde{\partial\Omega}_i = \partial\Omega_i \cap \partial\Omega$. We assume the interface to be planar in this work. We denote the outward-directed unit normal to

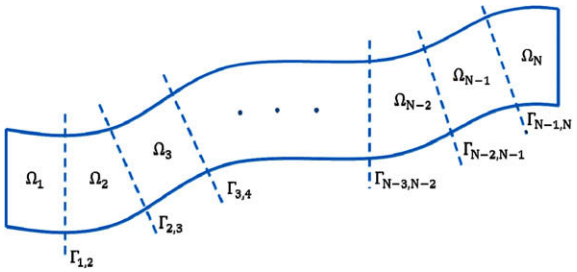

Fig. 1. One way decomposition of a large scale electromagnetic problem.

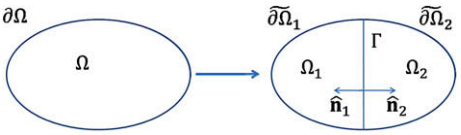

Fig. 2. Notation for decomposition of the domain.

$\partial\Omega_i$ by $\hat{\mathbf{n}}_i$. The subscripts $i = \in \{1,2\}$ will denote the restriction of a quantity to $\overline{\Omega}_i$. For example, in $\overline{\Omega}_i$, $\mathbf{E}_i$ will denote the electric field while ε_{ri} and μ_{ri} will denote the relative permittivity and permeability, respectively.

We will also use the tangential trace operator

$$\gamma_\tau(\mathbf{u}_i) := \hat{\mathbf{n}}_i \times \mathbf{u}_i|_{\partial\Omega_i} \tag{5}$$

and tangential components trace operator

$$\pi_\tau(\mathbf{u}_i) := \hat{\mathbf{n}}_i \times (\mathbf{u}_i \times \hat{\mathbf{n}}_i)|_{\partial\Omega_i} \tag{6}$$

We begin by defining a boundary value problem (BVP) for the decomposed problem of Fig. 2. It can be written as

$$\nabla \times \mu_{r1}^{-1} \nabla \times \mathbf{E}_1 - k_0^2 \varepsilon_{r1} \mathbf{E}_1 = -jk_0\eta_0 \mathbf{J}_1^{imp} \quad \text{in } \Omega_1 \tag{7}$$

$$\nabla \times \mu_{r2}^{-1} \nabla \times \mathbf{E}_2 - k_0^2 \varepsilon_{r2} \mathbf{E}_2 = -jk_0\eta_0 \mathbf{J}_2^{imp} \quad \text{in } \Omega_2 \tag{8}$$

$$\pi_\tau(\mathbf{E}_1) = \pi_\tau(\mathbf{E}_2) \quad \text{on } \Gamma \tag{9}$$

$$\gamma_r(\mu_{r1}^{-1} \nabla \times \mathbf{E}_1) = \gamma_\tau(\mu_{r2}^{-1} \nabla \times \mathbf{E}_2) \quad \text{on } \Gamma \tag{10}$$

$$\pi_\tau(\mathbf{E}_i) = 0 \quad \text{on } \Gamma_D \tag{11}$$

$$\gamma_\tau(\mu_{ri}^{-1} \nabla \times \mathbf{E}_i) = 0 \quad \text{on } \Gamma_N \tag{12}$$

$$\gamma_\tau(\mu_{ri}^{-1} \nabla \times \mathbf{E}_i) - jk_0 \sqrt{\frac{\varepsilon_{ri}}{\mu_{ri}}} \pi_\tau(\mathbf{E}_i) = 0 \quad \text{on } \widetilde{\partial\Omega_i} \tag{13}$$

for $i \in 1, 2$ and with $\mathbf{E}_i \in \mathbf{H}_0(\text{curl};\Omega_i)$ represents the electric field in a sub-domain. Note that $\mathbf{E}_1$ and $\mathbf{E}_2$ are allowed to be discontinuous on Γ. Eqs. (9) and (10) enforce the tangential continuity of the electric and magnetic fields of the otherwise unconstrained sub-domain fields. These conditions render the decomposed BVP above equivalent to the of the original problem domain Ω. Eqs. (11) and (12) give homogeneous Dirichlet and Neumann boundary conditions on the PEC surfaces, Γ_D and PMC surfaces, Γ_N, respectively. Finally, Eq. (13) is a first order absorbing boundary condition (ABC) on the exterior of the problem domain.

Here, our general interface conditions with second order derivatives in the transverse direction are presented as

$$\gamma_\tau(\mu_{r1}^{-1} \nabla \times \mathbf{E}_1) + \alpha\pi_\tau(\mathbf{E}_1) + \beta\nabla_\tau \times \mu_{r1}^{-1} \nabla_\tau \times \pi_\tau(\mathbf{E}_1) = -\gamma_\tau(\mu_{r2}^{-1} \nabla \times \mathbf{E}_2) + \alpha\pi_\tau(\mathbf{E}_2) + \beta\nabla_\tau \times \mu_{r2}^{-1} \nabla_\tau \times \pi_\tau(\mathbf{E}_2) \tag{14}$$

$$\gamma_\tau(\mu_{r2}^{-1} \nabla \times \mathbf{E}_2) + \alpha\pi_\tau(\mathbf{E}_2) + \beta\nabla_\tau \times \mu_{r2}^{-1} \nabla_\tau \times \pi_\tau(\mathbf{E}_2) = -\gamma_\tau(\mu_{r1}^{-1} \nabla \times \mathbf{E}_1) + \alpha\pi_\tau(\mathbf{E}_1) + \beta\nabla_\tau \times \mu_{r1}^{-1} \nabla_\tau \times \pi_\tau(\mathbf{E}_1) \tag{15}$$

with complex coefficients α and β to be determined. Straight-forward algebraic manipulation shows that the correct tangential field continuities of (9) and (10) are enforced if $\alpha \neq 0$. In the following section we show that the proper choice of parameters in this interface condition can improve the convergence for both propagation modes and evanescent modes.

2.3. Convergence analysis for the second order transmission conditions (SOTCs)

We will assess the convergence behavior of the DD algorithm which uses the SOTCs (14) and (15) by using an approach equivalent to the Fourier analysis of [10]. There, the convergence factors for coefficients of a stationary iterative algorithm are derived by making use of an idealized decomposition of $\mathbb{R}^3$ by the infinite plane $z = 0$. A rotation of the fields in the Fourier space leads to a decoupling of the transverse electric (TE) and transverse magnetic (TM) fields and simplifies the analysis in the Fourier domain.

We once again start by decomposing $\mathbb{R}^3$ into two semi-infinite domains with Γ defined to be the plane $z = 0$, $\Omega_1 = \mathbb{R}^2 \times (\infty, 0]$ and $\Omega_2 = \mathbb{R}^2 \times [0, \infty)$. To further simplify the analysis, we consider plane waves in free space traveling in the yz plane. The SOTCs are imposed on Γ and an iterative solution process is considered. We note that while this analysis is performed using a simplified problem, the results obtained correspond very well to the performance seen when applied to real-life engineering applications. The convergence factors of the iterative algorithm are determined as functions of the $\hat{\mathbf{z}}$ directed wave number k_z using a decomposition of the solution into TE and TM components. The magnitude of the convergence factor corresponds to the spectral radius (the maximum magnitude of the eigenvalues) of the DD algorithm operator. An operator with a spectral radius $\rho < 1$ is said to be convergent because a simple stationary iterative algorithm is guaranteed to converge to the solution. While this condition need not be met when using Krylov subspace iterative method, a small spectral is still preferable in order to provide rapid and robust convergence of the iterative method. The following interface iterations on Γ are used to derive our general convergence factors

Table 1
TE and TM field representations on the domain interface.

	Ω_1			Ω_2		
	$\pi_\tau(\mathbf{E}^{(n)})$	$\gamma_\tau(mu_r^{-1}\nabla\times\mathbf{E}^{(n)})$	$\nabla_\tau\times\mu_r^{-1}\nabla_\tau\times\pi_\tau(\mathbf{E}^{(n)})$	$\pi_\tau(\mathbf{E}^{(n)})$	$\gamma_\tau(\mu_\tau\nabla\times\mathbf{E}^{(n)})$	$\nabla_\tau\times\mu_r^{-1}\nabla_\tau\times\pi_\tau(\mathbf{E}^{(n)})$
TE	$\hat{\mathbf{x}}c_1^{(n)}e^{-jk_y y}$	$-\hat{\mathbf{x}}c_1^{(n)}jk_z e^{-jk_y y}$	$\hat{\mathbf{x}}c_1^{(n)}k_y^2 e^{-jk_y y}$	$\hat{\mathbf{x}}c_2^{(n)}e^{-jk_y y}$	$-\hat{\mathbf{x}}c_2^{(n)}jk_z e^{-jk_y y}$	$\hat{\mathbf{x}}c_2^{(n)}j_y^2 e^{-jk_y y}$
TM	$\hat{y}c_1^{(n)}\frac{k_z}{k}e^{-jk_y y}$	$-\hat{y}c_1 jke^{-jk_y y}$	0	$-\hat{y}c_2^{(n)}\frac{k_z}{k}e^{-jk_y y}$	$\hat{y}c_2^{(n)}jke^{-jk_y y}$	0

$$\gamma_\tau\left(\mu_{r1}^{-1}\nabla\times\mathbf{E}_1^{(n)}\right)+\alpha\pi_\tau(\mathbf{E}_1^{(n)})+\beta\nabla_\tau\times\mu_{r1}^{-1}\nabla_\tau\times\pi_\tau\left(\mathbf{E}_1^{(n)}\right)=-\gamma_\tau\left(\mu_{r2}^{-1}\nabla\times\mathbf{E}_2^{(n-1)}\right)+\alpha\pi_\tau\left(\mathbf{E}_2^{(n-1)}\right)+\beta\nabla_\tau\times\pi_\tau\left(\mathbf{E}_2^{(n-1)}\right) \tag{16}$$

$$\gamma_\tau\left(\mu_{r2}^{-1}\nabla\times\mathbf{E}_2^{(n)}\right)+\alpha\pi_\tau(\mathbf{E}_2^{(n-1)})+\beta\nabla_\tau\times\mu_{r2}^{-1}\nabla_\tau\times\pi_\tau\left(\mathbf{E}_2^{(n)}\right)=-\gamma\left(\mu_{r1}^{-1}\nabla\times\mathbf{E}_1^{(n-1)}\right)+\alpha\pi_\tau\left(\mathbf{E}_1^{(n-1)}\right)+\beta\nabla_\tau\times\pi_\tau\left(\mathbf{E}_1^{(n-1)}\right) \tag{17}$$

We first consider TE modes and the following solutions in each of the sub-domains:

$$\mathbf{E}_1^{(n)}=\hat{\mathbf{x}}c_1^{(n)}e^{-j(k_y y-k_z z)} \tag{18}$$

$$\mathbf{E}_2^{(n)}=\hat{\mathbf{x}}c_2^{(n)}e^{-j(k_y y+k_z z)} \tag{19}$$

where $c_1^{(n)}$ and $c_2^{(n)}$ are the excitation coefficients. For TM modes, the electric fields in the sub-domains are written as

$$\mathbf{E}_1^{(n)}=\frac{c_1^{(n)}}{k}(\hat{\mathbf{y}}k_z+\hat{\mathbf{z}}k_y)e^{-j(k_y y-k_z z)} \tag{20}$$

$$\mathbf{E}_2^{(n)}=\frac{c_2^{(n)}}{k}(-\hat{\mathbf{y}}k_z+\hat{\mathbf{z}}k_y)e^{-j(k_y y+k_z z)} \tag{21}$$

The field representations of Table 1 can be obtained through simple vector manipulation. Substitution of the quantities which corresponds to TE modes in Table 1 into (16) and (17) gives:

$$C_1^{(n)}(-jk_z+\alpha+\beta k_y^2)=c_2^{(n-1)}\left(jk_z+\alpha+\beta k_y^2\right) \tag{22}$$

$$C_2^{(n-1)}(-jk_z+\alpha+\beta k_y^2)=c_1^{(n-2)}\left(jk_z+\alpha+\beta k_y^2\right) \tag{23}$$

and we obtain the convergence factor

$$\rho_{\mathrm{TE}}=\left|\frac{c_1^{(n)}}{c_1^{(n-2)}}\right|=\left|\frac{jk_z+\alpha+\beta k_y^2}{-jk_z+\alpha+\beta k_y^2}\right|^2=\left|\frac{jk_z+\alpha+\beta(k^2-k_z^2)}{jk_z-\alpha-\beta(k^2-k_z^2)}\right|^2 \tag{24}$$

where we have made use of the dispersion relation $k^2-k_y^2+k_z^2$.

Similarly, we obtain the convergence factor for TM modes as

$$|\rho_{\mathrm{TM}}|=\left|\frac{k^2-j\alpha k_z}{k^2+j\alpha k_z}\right|^2 \tag{25}$$

2.3.1. First order transmission condition (FOTC)

By choosing $\beta=0$ and $\alpha=-jk_0$ we will obtain the first order Robin-type TC. This leads to the convergence factors

$$|\rho_{\mathrm{TE}}|=|\rho_{\mathrm{TM}}|=\left|\frac{k_z-k}{k_z+k}\right|^2 \tag{26}$$

We note that for propagating modes (real, positive k_z) we obtain $|\rho_{\mathrm{TE}}|=|\rho_{\mathrm{TM}}|<1$ while at cutoff ($k_z=0$) and for evanescent modes (imaginary k_z) we have $|\rho_{\mathrm{TE}}|=|\rho_{\mathrm{TM}}|=1$. Hence, the FOTC leads to convergence of propagating modes but not evanescent ones. The largest evanescent mode supported by the discretization increases with decreasing mesh size or increasing polynomial order. This is due to the increased ability of the higher order basis functions or finer mesh to represent the rapidly oscillating interface modes. Consequently, the performance of DD methods with a FOTC deteriorates drastically with very small elements on the domain interfaces. Fig. 3 depicts the convergence factors for the FOTC.

2.3.2. Second order transmission condition–TE type (SOTC–TE)

For the SOTC–TE, we still choose $\alpha=-jk_0$ to obtain the same convergence rate for all TE and TM propagating modes. Now we have an additional degree of freedom β for the second order tangential differential term. This parameter is chosen to accelerate the convergence for the TE evanescent modes. We do this because in the **E** field formulation used here, the electric

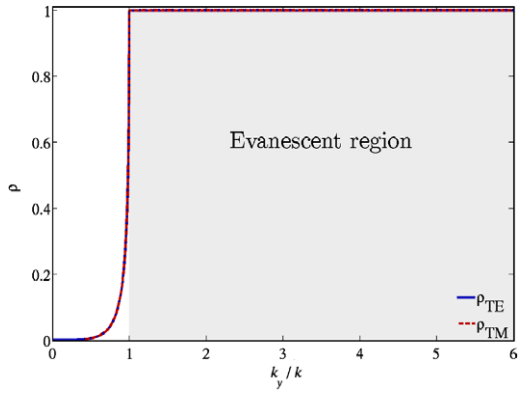

Fig. 3. Convergence factor of FOTC.

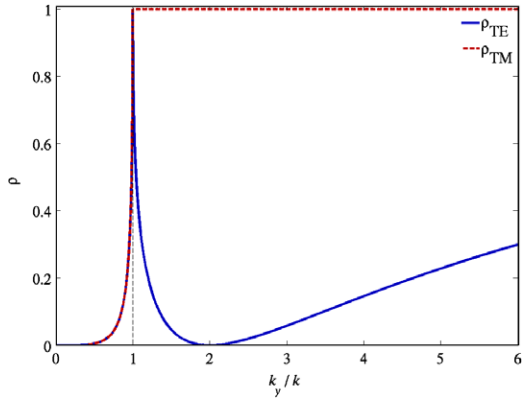

Fig. 4. Convergence factor of SOTC–TE.

field is represented to a greater accuracy than the magnetic field (which is obtained from the curl of E). Thus, higher oscillation is supported for the transverse electric field and the most troublesome evanescent modes are therefore of TE type.

The choice of β is made as follows. We let $k_\tau^{\max}$ denote the maximum transverse wave number supported by the numerical grid on Γ. In our implementation, we simply set $k_\tau^{\max} = \frac{\pi}{h_{\min}}$, where $h_{\min}$ is the minimum mesh size. According to the dispersion relation we have $\tilde{k}_z = -j\sqrt{(k_\tau^{max})^2 - k^2}$. By setting $\beta = \frac{j}{k+k_z}$, we obtain the convergence factors for TE and TM modes as

$$|\rho_{\mathrm{TE}}| = \left|\frac{(k-k_z)(\tilde{k}_z-k_z)}{(k+k_z)(\tilde{k}_z+k_z)}\right|^2 \tag{27}$$

$$|\rho_{\mathrm{TM}}| = \left|\frac{k_z-k}{k_z+k}\right|^2 \tag{28}$$

It can be shown that $|\rho_{\mathrm{TE}}| < 1$ for both propagating and evanescent TE modes. However, $|\rho_{\mathrm{TM}}| < 1$ only for propagating TM modes. For the evanescent TM modes, $|\rho_{\mathrm{TM}}| = 1$. The convergence factors are plotted in Fig. 4. It is seen in Fig. 4 that there are two zero values of convergence factor for TE modes, one in the propagating region and the other in the evanescent region.

2.3.3. Second order optimized transmission condition (SOTC–OPT)

By choosing $\alpha = -\frac{1}{p}k_0^2$ and $\beta = \frac{1}{p}$, we obtain the same interface conditions as presented in [17]. p is a complex number and $Re(p) > 0$ and $Im(p) > 0$. The convergence factors for TE and TM modes are obtained as following:

$$|\rho_{\mathrm{TE}}| = |\rho_{\mathrm{TM}}| = \left|\frac{jp+k_z}{jp-k_z}\right|^2 \tag{29}$$

Eq. (29) shows that the same convergence factors are obtained for both TE and TM modes and that the zero convergence value for the optimal TC occurs at $k_z = -jp$ for both TE and TM modes. However, the so-called optimal TC requires $Re(p) = Im(p)$ and thus does not provide zero convergence values for any pure propagating or evanescent mode. The parameter p is chosen by considering the size of the interface and the mesh size on the interface and is given by [18]

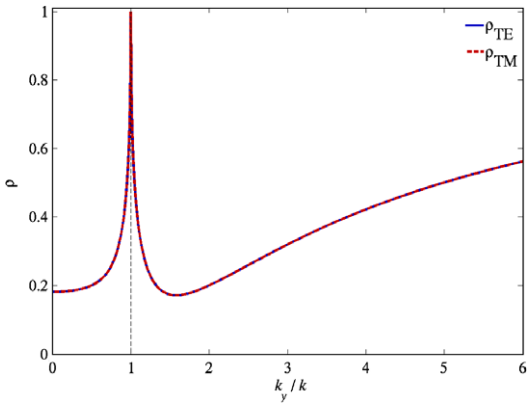

Fig. 5. Convergence factor of SOTC–OPT.

$$Re(p) = Im(p) = \frac{\sqrt{k_\tau^{\max}}[\min(k_+^2 - k_0^2, k_0^2 - k_-^2)]^{1/4}}{\sqrt{2}} \tag{30}$$

$$K_\tau^{\min} = 0\left(\frac{\pi}{l_{\max}}\right); k_\tau^{\max} = 0\left(\frac{\pi}{h_{\min}}\right); \quad k_- = k_0 - k_\tau^{\min}; \quad k_+ = k_0 + k_\tau^{\min} \tag{31}$$

where $k_\tau^{\min}$ denotes the smallest frequency relevant to the subdomain and $l_{\max}$ denotes the largest length of the sub-domain. The convergence factors are plotted in Fig. 5.

From Fig. 5 we see that for the SOTC–OPT, $|\rho_{TM}| = |\rho_{TE}| < 1$, for both propagating and evanescent TE and TM modes and it therefore damps both TE and TM evanescent modes. In theory, it is more robust than SOTC–TE. However, it is not always more efficient than the SOTC–TE. The damping of evanescent modes comes at the expense of less damping for both TE and TM propagating modes. It is expected that, the SOTC–OPT will perform better for problems with very small elements, while the second order TE will be the better choice when propagating modes dominate the spectrum. Numerical experiments supporting this analysis are presented in Section 3.

2.4. Weak formulation

We now turn to the weak formulation of the DD method to solve Eqs. (7)–(15). First, we define some mathematical notation and recall Sobolev spaces required for the formulation.

Volume and surface sesquilinear forms are defined by

$$(\mathbf{u}, \mathbf{v})_\Omega := \int_\Omega \bar{\mathbf{u}} \cdot \mathbf{v}\, dv$$

$$\langle \mathbf{u}, \mathbf{v} \rangle_{\partial\Omega} := \int_{\partial\Omega} \bar{\mathbf{u}} \cdot \mathbf{v}\, ds$$

where the over bar denotes conjugation. Note that we sometimes use $(\mathbf{u}, \mathbf{v})_\Omega$ to mean the broken form $(\mathbf{u}_1, \mathbf{v}_1)_{\Omega_1} + (\mathbf{u}_2, \mathbf{v}_2)_{\Omega_2}$ and, similarly, $\langle \mathbf{u}, \mathbf{v} \rangle_{\partial\Omega} = \langle \mathbf{u}_1, \mathbf{v}_2 \rangle_{\widetilde{\partial\Omega_1}} + \langle \mathbf{u}_2, \mathbf{v}_2 \rangle_{\widetilde{\partial\Omega_2}}$.

We recall the standard Sobolev spaces $H^s(\Omega)$ for $s \in \mathbb{R}$ and set

$$\mathbf{H}^s(\Omega) := (H^s(\Omega))^3$$

$$L^2(\Omega) := H^0(\Omega)$$

$$\mathbf{L}^2(\Omega) := \mathbf{H}^0(\Omega)$$

Also we define

$$\mathbf{H}(\mathrm{curl};\Omega) := \{\mathbf{u} \in \mathbf{L}^2(\Omega) | \nabla \times \mathbf{u} \in \mathbf{L}^2(\Omega)\}$$

$$\mathbf{H}(\mathrm{div};\Omega) := \{\mathbf{u} \in \mathbf{L}^2(\Omega) | \nabla \cdot \mathbf{u} \in L^2(\Omega)\}$$

$$\mathbf{H}^{-1/2}(\mathrm{curl}_\tau;\partial\Omega) := \{\mathbf{u} \in \mathbf{H}^{-1/2}(\partial\Omega) | \hat{\mathbf{n}} \cdot (\nabla_\tau \times \mathbf{u}) \in H^{-1/2}(\partial\Omega), \hat{\mathbf{n}} \cdot \mathbf{u} = 0\}$$

$$\mathbf{H}^{-1/2}(\mathrm{div}_\tau;\partial\Omega) := \{\mathbf{u} \in \mathbf{H}^{-1/2}(\partial\Omega) | \nabla_\tau \cdot \mathbf{u} \in H^{-1/2}(\partial\Omega), \hat{\mathbf{n}} \cdot \mathbf{u} = 0\}$$

$$\mathbf{H}_0(\mathrm{curl};\Omega) := \{\mathbf{u} \in \mathbf{H}(\mathrm{curl};\Omega) | \gamma_\tau(\mathbf{u}) = 0 \text{ on } \Gamma_D\}$$

Note that $\mathbf{H}_0(\mathrm{curl};\Omega)$ is the space of curl-conforming functions that satisfy essential boundary conditions on Γ_D, the collection of surfaces on which Dirichlet boundary conditions are applied. This is the space in which the electric field resides with

the appropriate Dirichlet conditions {e.g. Perfect Electrically Conducting (PEC)]. That is, we may write $\mathbf{E}_i \in \mathbf{H}_0(\mathrm{curl};\Omega_i)$ where the two spaces are understood to have different Dirichlet boundary conditions. Finally, we recall that the function spaces for the traces of curl-conforming functions are given

$$\mathbf{H}^{-1/2}(\mathrm{curl}_\tau;\partial\Omega) := \{\pi_\tau(\mathbf{u})|\mathbf{u} \in \mathbf{H}(\mathrm{curl};\Omega)\}$$
$$\mathbf{H}^{-1/2}(\mathrm{div}_\gamma;\partial\Omega) := \{\pi_\tau(\mathbf{u})|\mathbf{u} \in \mathbf{H}(\mathrm{curl};\Omega)\}$$

and that

$$\mathbf{H}(\mathrm{curl};\Omega)' = \mathbf{H}(\mathrm{div};\Omega)$$
$$\mathbf{H}^{-1/2}(\mathrm{curl}_\tau;\partial\Omega)' = \mathbf{H}^{-1/2}(\mathrm{div}_\tau;\partial\Omega)$$

where $\mathbf{x}'$ denotes the function space dual to $\mathbf{X}$ in the appropriate L^2 inner product.

Here, we rewrite our TCs in a slightly different form and note that, for a non-singular operator $\mathcal{L}$, we may equivalently express the tangential continuity conditions of (9) and (10) via the TCs

$$\gamma_\tau(\mu_{r1}^{-1}\nabla\times\mathbf{E}_1) + \mathcal{L}(\pi_\tau(\mathbf{E}_1)) = -\gamma_\tau(\mu_{r2}^{-1}\nabla\times\mathbf{E}_2) + \mathcal{L}(\pi_\tau(\mathbf{E}_2)) \tag{32}$$
$$\gamma_\tau(\mu_{r2}^{-1}\nabla\times\mathbf{E}_2) + \mathcal{L}(\pi_\tau(\mathbf{E}_2)) = -\gamma_\tau(\mu_{r1}^{-1}\nabla\times\mathbf{E}_1) + \mathcal{L}(\pi_\tau(\mathbf{E}_1)) \tag{33}$$

We will consider three operators to define the TCs. The first, $\mathcal{L}_1$, is an imaginary scaling factor that results in the usual complex first order Robin TC for non-overlapping domain decomposition. The second operator, $\mathcal{L}_{\mathrm{TE}}$, gives the SOTC–TE. The final operator $\mathcal{L}_{\mathrm{OPT}}$, is the SOTC–OPT proposed in [17].

We write the three operators as

$$\mathcal{L} := \alpha$$
$$\mathcal{L}_{\mathrm{TE}} := \alpha + \beta\nabla_\tau\times\mu_r^{-1}\nabla_\tau\times$$
$$\mathcal{L}_{OPT} := -\frac{1}{p}(\nabla_\tau\times\mu_r^{-1}\nabla_\tau\times - k_0^2\varepsilon_r)$$

To implement the DD algorithm, we introduce an auxiliary variable. This interface variable is defined as

$$\lambda_i := \gamma_\tau(\mu_{ri}^{-1}\nabla\times\mathbf{E}_i) - \mathcal{L}(\pi_\tau(\mathbf{E}_i)) \tag{34}$$

The TCs can now be written using the auxiliary variable as

$$\lambda_1 + 2\mathcal{L}(\pi_\tau(\mathbf{E}_1)) + \lambda_2 = 0 \tag{35}$$
$$\lambda_2 + 2\mathcal{L}(\pi_\tau(\mathbf{E}_2)) + \lambda_1 = 0 \tag{36}$$

In what follows, we will abuse the notation somewhat and split Γ into Γ_{12}, the interface as seen from Ω_1, and Γ_{21}, the interface as seen from Ω_2. We do so in order to include the case where interface meshes of the discrete method do not match.

We then test Eqs. (7) and (8) using curl-conforming functions $\mathbf{w}_i \in \mathbf{H}_0(\mathrm{curl};\Omega_i), i \in \{1,2\}$ to give (after an integration by parts)

$$(\nabla\times\mathbf{w}_i, \mu_{ri}^{-1}\nabla\times\mathbf{E}_i)_{\Omega_i} - k_0^2(\mathbf{w}_i, \varepsilon_{ri}\mathbf{E}_i)_{\Omega_i} + \langle(\pi_\tau(\mathbf{w}_i), \gamma_\tau(\mu_{ri}^{-1}\nabla\times\mathbf{E}_i)\rangle_\Gamma = -jk_0\eta_0\left(\mathbf{w}_i, \mathbf{J}_i^{\mathrm{imp}}\right)_{\Omega_i} \tag{37}$$

where we have ignored the treatment of the exterior boundary for simplicity. Now, using (34) we obtain

$$(\nabla\times\mathbf{w}_i, \mu_{ri}^{-1}\nabla\times\mathbf{E}_i)_{\Omega_i} - k_0^2(\mathbf{w}_i, \varepsilon_{ri}\mathbf{E}_i)_{\Omega_i} + \langle\pi_\tau(\mathbf{w}_i), \mathcal{L}(\pi_\tau(\mathbf{E}_i))\rangle_{\Gamma_{ij}} + \langle\pi_\tau(\mathbf{w}_i), \lambda_i\rangle_{\Gamma_{ij}} = -jk_0\eta_0\left(\mathbf{w}_i, \mathbf{J}_i^{\mathrm{imp}}\right)_{\Omega_i} \tag{38}$$

We choose to represent the auxiliary variables λ_i, in a properly chosen space $\mathbf{H}_0^{-1/2}(\mathrm{curl}_\tau;\Gamma_{ij})$. We write $\lambda_i \in \mathbf{H}_0^{-1/2}(\mathrm{curl}_\tau;\Gamma_{ij})$ and choose test function v_i from the same space. Then, we test Eqs. (35) and (36) with the v_i to obtain

$$\langle v_i, \lambda_i\rangle_{\Gamma_{ij}} + 2\langle v_i, \mathcal{L}(\pi_\tau(\mathbf{E}_i))\rangle\Gamma_{ij} + \langle v_i, \lambda_i\rangle_{\Gamma_{ij}} = 0$$
$$\forall i,j \in \{1,2\}, \quad i \neq j. \tag{39}$$

The final weak form for the two domain problem is then given by:

Seek $(\mathbf{E}_1,\mathbf{E})_2 \in \mathbf{H}_0(\mathrm{curl};\Omega_1)\times\mathbf{H}_0(\mathrm{curl};\Omega_2), (\lambda_1,\lambda_2) \in \mathbf{H}_0^{-1/2}(\mathrm{curl}_\tau;\Gamma_{12})\times\mathbf{H}_0^{-1/2}(\mathrm{curl}_\tau;\Gamma_{21})$, such that

$$(\nabla\times\mathbf{w}_1, \mu_{r1}^{-1}\nabla\times\mathbf{E}_1)_{\Omega_1} - k_0^2(\mathbf{w}_1, \varepsilon_{r1}\mathbf{E}_1)_{\Omega_2} + \langle\pi_\tau(\mathbf{w}_1), \mathcal{L}(\pi_\tau(\mathbf{E}_1))\rangle_{\Gamma_{12}} + \langle\pi_\tau(\mathbf{w}_1), \lambda_1\rangle_{\Gamma_{12}} = -jk_0\eta_0(\mathbf{w}_1\mathbf{J}_1^{\mathrm{imp}})_{\Omega_1} \tag{40}$$
$$(\nabla\times\mathbf{w}_2, \mu_{r2}^{-1}\nabla\times\mathbf{E}_2)_{\Omega_2} - k_0^2(\mathbf{w}_2\varepsilon_{r2}\mathbf{E}, \mathbf{E})_{\Omega_2} + \langle\pi_\tau(\mathbf{w}_2), \mathcal{L}(\pi_\tau(\mathbf{w}_2))\rangle_{\Gamma_{21}} + \langle\pi_\tau(\mathbf{w}_2), \lambda_2\rangle_{\Gamma_{21}} = -jk_0\eta_0\left(\mathbf{w}_2, \mathbf{J}_2^{\mathrm{imp}}\right)_{\Omega_2} \tag{41}$$
$$\langle v_1, \lambda_1\rangle_{\Gamma_{12}} + 2\langle v_1, \mathcal{L}(\pi_\tau(\mathbf{E}_1))\rangle_{\Gamma_{12}} + \langle v_1, \lambda_2\rangle_{\Gamma_{12}} = 0 \tag{42}$$
$$\langle v_1, \lambda_2\rangle_{\Gamma_{P_{21}}} 2\langle v_2, \mathcal{L}(\pi_\tau(\mathbf{E}_2))\rangle_{\Gamma_{12}} + \langle v_2, \lambda_1\rangle_{\Gamma_{21}} = 0 \tag{43}$$

$\forall(\mathbf{w}_1,\mathbf{w}_2) \in \mathbf{H}_0 \in \mathbf{H}_0(\mathrm{curl};\Omega_1)\times\mathbf{H}_0(\mathrm{curl};\Omega_1), (v_1,v_2) \in \mathbf{H}_0^{-1/2}(\mathrm{curl}_\tau;\Gamma_{12})\times\mathbf{H}_0^{-1/2}(\mathrm{curl}_\tau;\Gamma_{21})$.

2.5. Discrete formulation

We now introduce independent tetrahedral meshes, $\mathcal{K}_i$, in each region Ω_i. The surface meshes induced on Γ_{ij} is denoted by $\mathcal{T}_{ij}$ On each of the sub-domain, we define discrete trial and test functions, $\mathbf{E}_i^h \in \mathbf{X}_i^h$ and $\mathbf{w}_i^h \in \mathbf{X}_i^h$ respectively, with $\mathbf{X}_i^h \subset \mathbf{H}_0(\mathrm{curl};\Omega_i)$. Here, $\mathbf{X}_i^h$ is taken to be the space of basis functions defined [20], with order $p = 2$. On the interfaces, we also define discrete trial and test functions, $\boldsymbol{\lambda}_i^h \in \mathbf{Y}_i^h$ and $\boldsymbol{\nu}_i^h \in \mathbf{Y}_i^h$, respectively, with $\mathbf{Y}_i^h \subset \mathbf{H}^{-1/2}(\mathrm{curl}_\tau;\Gamma_{ij})$. $\mathbf{y}_I^H$ will be taken as the two-dimensional restriction of $\mathbf{X}_i^h$, but with DOFs defined independently where appropriate.

We may now write the discrete DD method as:

Seek $(\mathbf{E}_1^h,\mathbf{E})_2^h \in \mathbf{X}_1^h \times \mathbf{X}_2^{\mathbf{h}}, (\lambda_1^h,\lambda_2^h) \in \mathbf{Y}_1^h \times \mathbf{Y}_2^h$, such that

$$\left(\nabla\times\mathbf{w}_1^h,\mu_{r1}^{-1}\nabla\times\mathbf{E}_1^h\right)_{\mathcal{K}_1} - k_0^2(\mathbf{w}_1^h,\varepsilon_{r1}\mathbf{E}_1^h)_{\mathcal{K}_1} + \langle\pi_\tau(\mathbf{w}_1^h),\mathcal{L}\left(\pi_\tau(\mathbf{E}_1^h)\right)\rangle_{\mathcal{J}_{12}} + \langle\pi_\tau(\mathbf{w}_1^h),\lambda_1^h\rangle_{\mathcal{J}_{12}} = -jk_0\eta_0(\mathbf{w}_1^h,\mathbf{J}_1^{\mathrm{imp}})_{\mathcal{K}_1} \tag{44}$$

$$\left(\nabla\times\mathbf{w}_2^h,\mu_{r2}^{-1}\nabla\times\mathbf{E}_2^h\right)_{\mathcal{K}_2} - k_0^2\left(\mathbf{w}_2^h,\varepsilon_{r2}\mathbf{E}_2^h\right)_{\mathcal{K}_2} + \langle\pi_\tau(\mathbf{w}_2^h),\mathcal{L}\left(\pi_\tau\mathbf{E}_2^h\right)_{\mathcal{J}_{21}} + \langle\pi_\tau(\mathbf{w}_2^h),\boldsymbol{\lambda}_2^h\rangle_{\mathcal{J}_{21}} = -jk_0\eta_0\left(\mathbf{w}_2^h,\mathbf{J}_2^{\mathrm{imp}}\right)_{\mathcal{K}_2} \tag{45}$$

$$\langle\boldsymbol{\nu}_i^h,\boldsymbol{\lambda}_1^h\rangle_{\mathcal{J}_{12}} + 2\langle\boldsymbol{\nu}_1^h,\mathcal{L}\left(\pi_\tau(\mathbf{E}_1^h)\right)_{\mathcal{J}_{12}} + \langle\boldsymbol{\nu}_1^h,\boldsymbol{\lambda}_2^h\rangle_{\mathcal{J}_{12}} = 0 \tag{46}$$

$$\langle\boldsymbol{\nu}_2^h,\boldsymbol{\lambda}_2^h\rangle_{\mathcal{J}_{21}} + 2\langle\boldsymbol{\nu}_2^h,\mathcal{L}\left(\pi_\tau(\mathbf{E}_2^h)\right)\rangle_{\mathcal{J}_{21}} + \langle\boldsymbol{\nu}_2^h,\boldsymbol{\lambda}_1^h\rangle_{\mathcal{J}_{21}} = 0 \tag{47}$$

$$\forall(\mathbf{w}_1^h,\mathbf{w}_2^h) \in \mathbf{X}_1^h \times \mathbf{X}_2^h, (\nu_1^h,\nu_2^h) \in \mathbf{Y}_1^h \times \mathbf{Y}_2^h.$$

Now we may write the matrix equation to be solved as

$$\begin{bmatrix} A_1^{II} & A_1^{I\Gamma} & 0 & 0 & 0 & 0 \\ A_1^{\Gamma I} & A_1^{\Gamma\Gamma}+B_1 & D_1 & 0 & 0 & 0 \\ 0 & C_1 & T_{11} & 0 & 0 & T_{12} \\ 0 & 0 & 0 & A_2^{II} & A_2^{I\Gamma} & 0 \\ 0 & 0 & 0 & A_2^{\Gamma I} & A_2^{\Gamma\Gamma}+B_2 & D_2 \\ 0 & 0 & T_{21} & 0 & C_2 & T_{22} \end{bmatrix} \begin{bmatrix} E_1 \\ e_1 \\ \lambda_1 \\ E_2 \\ e_2 \\ \lambda_2 \end{bmatrix} \begin{bmatrix} y_1 \\ 0 \\ 0 \\ y_2 \\ 0 \\ 0 \end{bmatrix} \tag{48}$$

where the block matrices and vectors are given by

$$A_i := (\nabla\times\mathbf{w}_i^h,\mu_{ri}^{-1}\nabla\times\mathbf{w}_i^h)_{\mathcal{K}_i} = k_0^2(\mathbf{w}_i^h,\varepsilon_{r1}\mathbf{w}_i^h)_{\mathcal{K}_i} \tag{49}$$

$$B_i := \langle\pi_\tau(\mathbf{w}_i^h),\mathcal{L}(\pi_\tau(\mathbf{w}_i^h))\rangle_{\mathcal{J}_{ij}} \tag{50}$$

$$C_i := 2\langle\boldsymbol{\nu}_i^h,\mathcal{L}(\pi_\tau(\mathbf{w}_i^h))\rangle_{\mathcal{J}_{ij}} \tag{51}$$

$$D_i := \langle\pi_\tau(\mathbf{w}_i^h),\boldsymbol{\lambda}_i\rangle_{\mathcal{J}_{ij}} \tag{52}$$

$$T_{ij} := \langle\boldsymbol{\nu}_i^h,\boldsymbol{\nu}_j^h\rangle_{\mathcal{J}_{ij}} \tag{53}$$

$$y_i := -jk_0\eta_o(\mathbf{w}_i^h,\mathbf{J}_i^{\mathrm{imp}})_{\mathcal{K}_i} \tag{54}$$

and E_i represents the electric field DOFs which are interior to the sub-domain, e_i represents the electric field DOFs with non-zero tangential component on Γ, and λ_i represents the DOFs for the auxiliary variable.

The matrices B_i and C_i depend upon the TC operators and they will be denoted by a subscript corresponding to the appropriate TC operator.

For example, for the first order TC operator we obtain

$$B_{i,\mathrm{FOTC}} = \langle\pi_\tau(\mathbf{w}_i^h),\alpha\pi_\tau(\mathbf{w}_i^h)\rangle_{\mathcal{J}_{ij}} \tag{55}$$

$$C_{i,\mathrm{FOTC}} = 2\langle\boldsymbol{\nu}_i^h,\alpha\pi_\tau(\mathbf{w}_i^h)\rangle\mathcal{J}_{ij} \tag{56}$$

For the second order TE operator, we have

$$B_{i,\mathrm{SOTC-TE}} = \langle\pi_\tau(\mathbf{w}_i^h),\alpha\pi_\tau(\mathbf{w}_i^h)\rangle_{\mathcal{J}_{ij}} + \langle\nabla_\tau(\mathbf{w}_i^h),\beta\nabla_\tau\times\pi_\tau(\mathbf{w}_i^h)\rangle_{\mathcal{J}_{ij}} \tag{57}$$

$$C_{i,\mathrm{SOTC-TE}} = 2\langle\boldsymbol{\nu}_i^h,\alpha\pi_\tau(\mathbf{w}_i^h)\rangle_{\mathcal{J}_{ij}} + 2\langle\nabla_\tau\times\nu_i^h,\beta\nabla_\tau\times\pi_\tau(\mathbf{w}_i^h)\rangle_{\mathcal{J}_{ij}} \tag{58}$$

Finally, for the second order optimal TC,

$$B_{i,\mathrm{SOTC-OPT}} = \langle\pi_\tau(\mathbf{w}_i^h),\frac{k_0^2}{p}\pi_\tau(\mathbf{w}_i^h)\rangle_{J_{ij}} + \langle\nabla_\tau\times\pi_\tau(\mathbf{w}_i^h),\frac{1}{p}\nabla_\tau\times\pi_\tau(\mathbf{w}_i h)\rangle_{\mathcal{J}_{ij}} \tag{59}$$

$$C_{i,\mathrm{SOTC-OPT}} = 2\langle\boldsymbol{\nu}_i^h,\frac{k_0^2}{p}\pi_\tau(\mathbf{w}_i^h)\rangle_{J_{ij}} + 2\langle\nabla_\tau\times\nu_i^h,\frac{1}{p}\nabla_\tau\times\pi_\tau(\mathbf{w}_i^h)\rangle_{\mathcal{J}_{ij}} \tag{60}$$

We will solve the matrix (49) via the FETI-like procedure of [13]. This involves the computation of a numerical Green's function for each of the sub-blocks of the problem geometry. Here, we refer to blocks as unique, possibly repeated, sub-structures

in the problem domain. A single numerical Green's function needs to be computed for each sub-block and may be re-used for all sub-domains sharing that geometry. The interested reader if referred to [10,13,19] for a detailed explanation of the solution algorithm. It is also worth noting that one advantage of this implementation is that the coupling matrix is much smaller than the previous version [10,13,19]. We direct interested readers to a recent Ph.D. dissertation for full and detail discussions on the implementation in Ref. [22].

We may write the matrix Eq. (49) to be solved as

$$\begin{pmatrix} A_1 & C_{12} \\ C_{21} & A_2 \end{pmatrix} \begin{pmatrix} x_1 \\ x_2 \end{pmatrix} = \begin{pmatrix} b_1 \\ b_2 \end{pmatrix} \tag{61}$$

where the matrices and vectors are given by

$$A_i = \begin{pmatrix} A_i^{II} & A_i^{I\Gamma} & 0 \\ A_i^{\Gamma I} & A_i^{\Gamma\Gamma} + B_i & D_i \\ 0 & C_i & T_{ii} \end{pmatrix} \tag{62}$$

$$C_{ij} = \begin{pmatrix} 0 & 0 & 0 \\ 0 & 0 & 0 \\ 0 & 0 & T_{ij} \end{pmatrix} \tag{63}$$

$$x_i = \begin{pmatrix} E_i \\ e_i \\ \lambda_i \end{pmatrix} \tag{64}$$

$$B_i = \begin{pmatrix} y_i \\ 0 \\ 0 \end{pmatrix} \tag{65}$$

By writing a block-Jacobi splitting of the system matrix (62) as

$$A = \begin{pmatrix} A_1 & 0 \\ 0 & A_2 \end{pmatrix} - \begin{pmatrix} 0 & -C_{12} \\ -C_{21} & 0 \end{pmatrix} = M - N \tag{66}$$

where $M = \begin{pmatrix} A_1 & 0 \\ 0 & A_2 \end{pmatrix}$ and $N = \begin{pmatrix} 0 & -C_{12} \\ -C_{21} & 0 \end{pmatrix}$. The Jacobi preconditioned system as

$$M^{-1}A = M^{-1}(M - N) = 1 - M^{-1}N \tag{67}$$

The convergence factors derived in Section 2.3 predict the eigenvalue distribution of matrix $M^{-1}N$. The eigenvalues of the matrix $M^{-1}A$ reside in a unit circle centered at one, due to the shift provided by the identity matrix.

3. Numerical experiment

In this Section, we first examine the eigenspectra of the preconditioned matrices obtained using the three TCs under consideration. Then we examine the performance of the three DD algorithms by examining their scalability with respect to certain parameters of interest. Lastly, we solve several problems of practical interest to demonstrate the superiority of one of the second TCs over the conventional Robin TC.

We will use a relative residual defined as

$$\varepsilon = \frac{\|M^{-1}(Ax - b)\|_2}{\|M^{-1}b\|_2} \tag{68}$$

where M is the FETI preconditioner, A is the DD matrix, and b is the excitation vector, and x is the solution at the current iteration. We note that although we solve the matrix equations to a relative residual $\varepsilon = 10^{-8}$, higher tolerances of $\varepsilon = 10^{-2}$ or $\varepsilon = 10^{-3}$ are often sufficient in practice. The ability to quickly converge to low tolerances is a good indicator of the robustness of the method.

3.1. Eigenspectra of the DD matrices

We will use a $\lambda_0/3$ segment of an X-band (WR-90) rectangular waveguide operated above cutoff for only the TE_{10} mode at 10 GHz. The geometry of the waveguide is depicted in Fig. 6. Here λ_0 is the wavelength in free space. Both ends of the waveguide are terminated by a first order ABC. The waveguide is partitioned by a transverse plane into two equally sized sub-domains that are meshed independently and quasi-uniformly such that the interface meshes do not match. Two

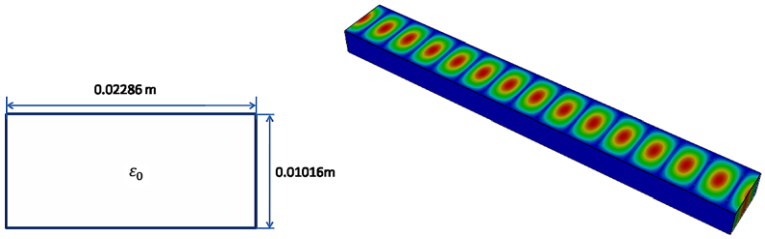

Fig. 6. A WR-90 waveguide (a) cross section; (b) the electric fields at 10 GHz.

Table 2
Choices of β and p versus different mesh sizes.

	h_{min} (m)	k_τ^{max}	β (SOTC–TE)	p (SOTC–OPT)
$h = \lambda_0/4$	0.00615	510.828	(−0.16833, −0.37416)	(201.036, 201.036)
$h = \lambda_0/8$	0.00312	1007.725	(−0.04330, −0.20351)	(282.296, 282.296)
$h = \lambda_0/12$	0.00187	1680.261	(−0.01556, −0.12380)	(364.607, 364.607)
$h = \lambda_0/16$	0.00138	2280.463	(−0.00845, −0.09150)	(424.764, 424.764)

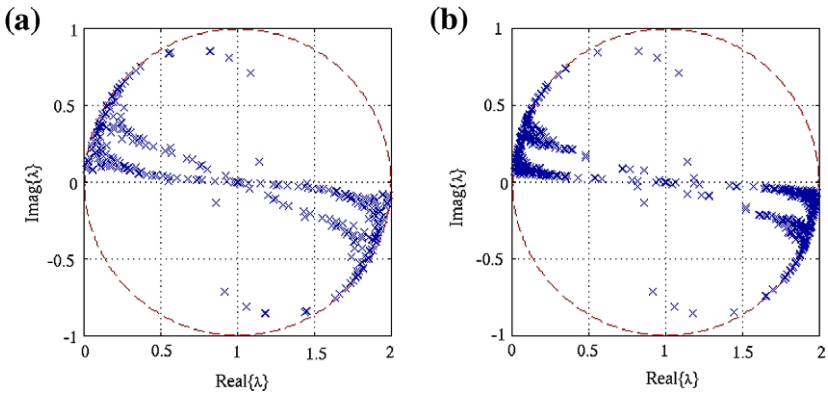

Fig. 7. Eigenspectra of FOTC for a WR-90 waveguide (a) $h = \lambda_0/8$; (b) $h = \lambda_0/12$.

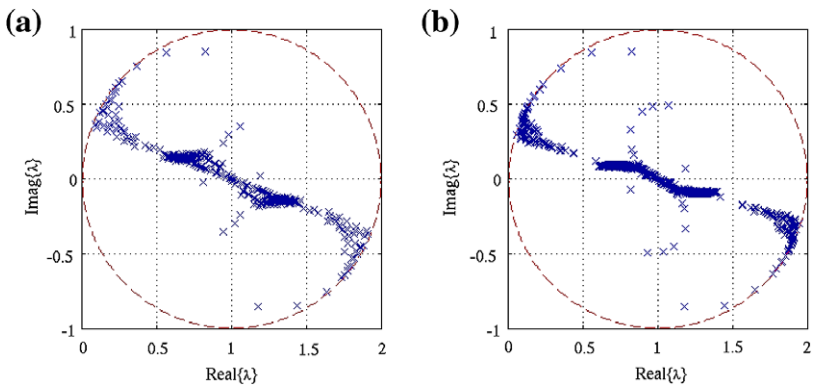

Fig. 8. Eigenspectra of SOTC–TE for a WR-90 waveguide (a) $h = \lambda_0/8$; (b) $h = \lambda_0/12$.

different mesh sizes, $h = \lambda_0/8$ and $\lambda_0/12$, are used to study the eigenspectra of the block-Jacobi preconditioned matrix of (49) for FOTC, SOTC–TE and SOTC–OPT, respectively. Table 2 presents the choices of β and p for SOTC–TE and SOTC–OPT with different mesh sizes. Here k_- and k_+ in Eq. (31) are chosen as 137.428 and 274.855, which are corresponding to TE_{10} and TE_{20} modes, respectively. Same parameters are used in the convergence study in Section 3.2.

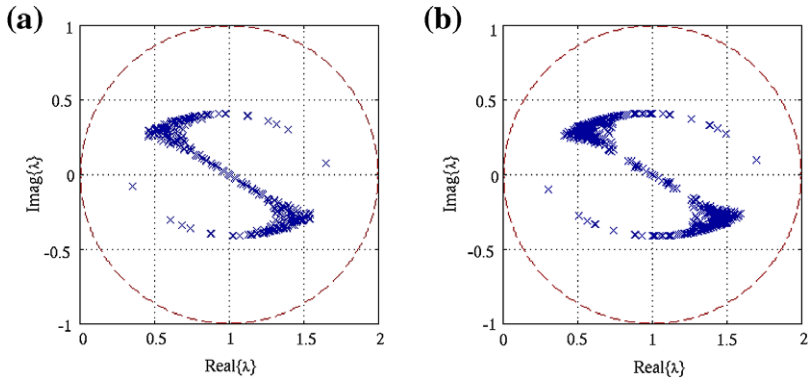

Fig. 9. Eigenspectra of SOTC–OPT for a WR-90 waveguide (a) $h = \lambda_0/8$; (b) $h = \lambda_0/12$.

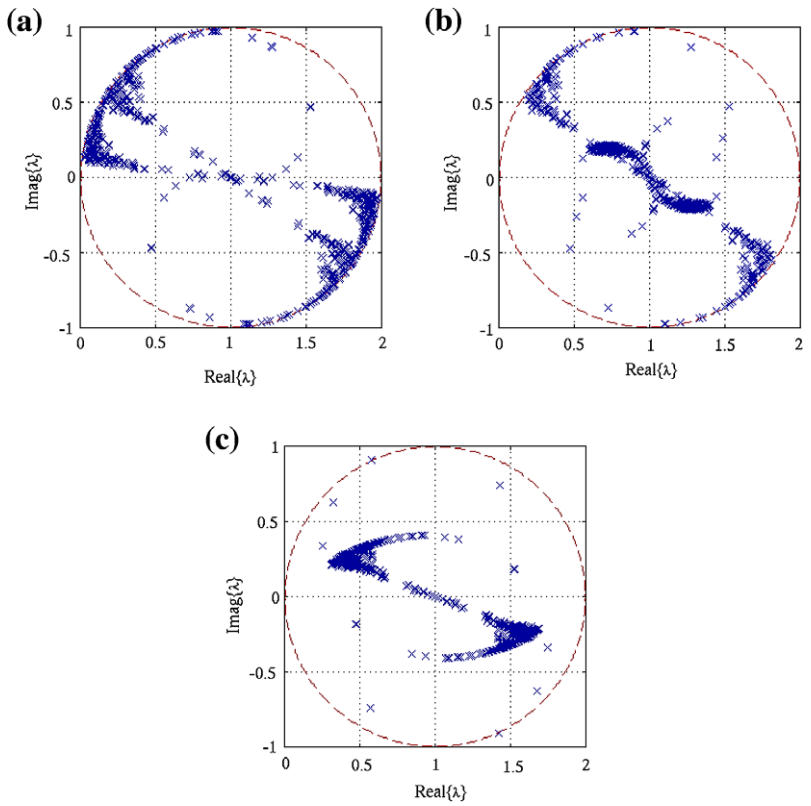

Fig. 10. Eigenspectra of for a WR-90 waveguide at 20 GHz (a) FOTC; (b) SOTC–TE; (c) SOTC–OPT.

First we examine the eigenspectra of the DD method with FOTC. From Fig. 7 we can see that many eigenvalues, those corresponding to evanescent modes, lie on the shifted unit circle. As the mesh is refined, the number of evanescent modes increases and the eigenvalues quickly approach zero. These small but non-zero eigenvalues will significantly degrade the performance of iterative Krylov subspace method. The remaining eigenvalues within the unit circle are the mixed modes. Because the non-conformity of the mesh allows coupling between propagating and evanescent modes on the interface, resulting in mixed modes which are neither purely propagation, nor evanescent. These modes have $|\rho| < 1$ even for FOTC.

It is worth to note that there are four clusters near the unit circle and two bands of eigenvalues connecting the anti-symmetric counterparts. The set that is nearer to the real axis corresponds to the TE modes while the other set corresponds to the TM modes. This is readily seen by examining Fig. 8 where, when the SOTC–TE is used, one of the two sets (the one corresponding to TE evanescent modes) is significantly altered.

For the SOTC–TE, the TE evanescent modes are brought well within the shifted unit circle and the eigenvalues are clustered in the center. We also note that the other set (the TM evanescent modes) remains unchanged. This comes as no surprise

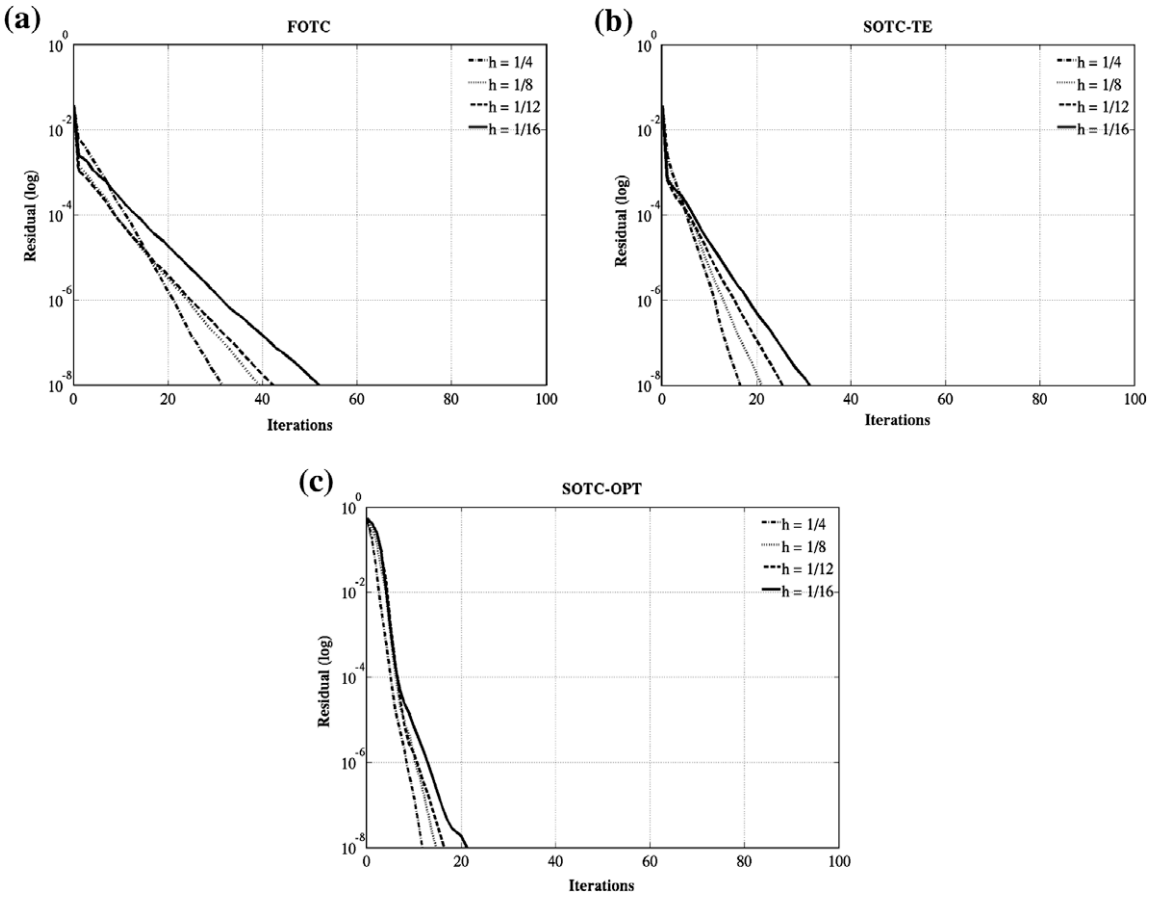

Fig. 11. Iterative solver convergence for a WR-90 waveguide with *h*-refinement (a) FOTC; (b) SOTC–TE; (c) SOTC–OPT.

since SOTC–TE does nothing to improve the TM modes. This is in agreement with the analysis in Section 2.3.2. Note that the evanescent modes with very small but non-zero eigenvalues are those that significantly degrade the performance of iterative Krylov subspace method. By decreasing the mesh size, both TE and TM evanescent modes move along the unit circle towards the origin, but the effect of TM modes is to a much lesser degree than TE ones. There fore the TM evanescent modes have far less impact on solver convergence than TE ones. As SOTC–TE takes care of the most troublesome TE evanescent modes, it is very effective in improving the condition number of the DD matrix in many practical applications.

Next, we see in Fig. 9 that, in agreement with the theory of Section 2.3.3, the SOTC–OPT provides convergence for all TE and TM propagating and evanescent modes. In this case, all eigenvalues are within the unit circle. The clustering of eigenvalues some fixed distance from one, is due to the fact the convergence of purely propagating and evanescent modes is limited by the minima of the curves of Fig. 4. The mixed modes however, show convergence better that these minima.

We now increase the frequency to $f = 20$ GHz and repeat the analysis. At this operating frequency, both TE_{11} and TM_{11} modes propagate. From Fig. 10 we also notice that, at this higher frequency, the behavior of SOTC–TE and SOTC–OPT consistent with that discussed above. In this study, k_- and k_+ in Eq. (31) are chosen as 413.712 and 515.353, which are corresponding to TE_{21} and TE_{31} modes, respectively.

3.2. Convergence study

The same WR-90 rectangular waveguide operated at 10 GHz is used for the following study. We are first concerned with the solver behavior as the mesh size, *h*, is reduced. This is of great interest as the accuracy of the method, as in the conventional FEM, can be controlled by refining the mesh. We use a segment of waveguide divided into five sub-domains of length $2\lambda_0/15$. The cross section this waveguide is $0.762\lambda_0 \times 0.339\lambda_0$. The mesh size is varied from $h = \lambda_0/4$ to $\lambda_0/16$ and the convergence of the GCR(10) solver is observed. Fig. 11(a) and (b) demonstrate that the FOTC and SOTC–TE are somewhat dependent upon mesh size, though the SOTC–TE demonstrates a considerable improvement in convergence. Fig. 11c demonstrates that the SOTC–OPT is quite insensitive to mesh size. This behavior can be explained by the fact that mesh refinement leads to an increase in evanescent modes on the interfaces. The FOTC does nothing to damp these modes while the SOTC–TE only

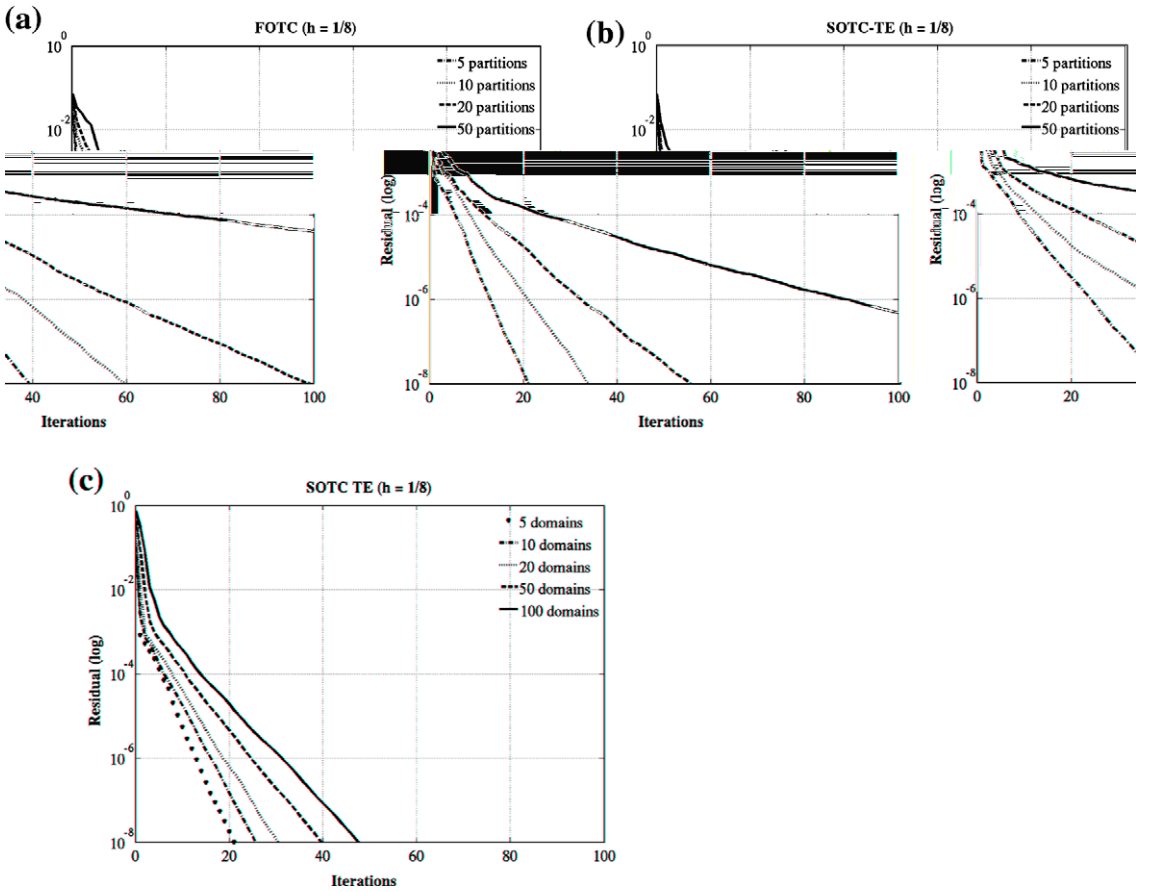

Fig. 12. Iterative solver convergence for a WR-90 waveguide with reduced sub-domain size (a) FOTC; (b) SOTC–TE; (c) SOTC–OPT.

damps a portion of the spectrum. The SOTC–OPT deals effectively with both TE and TM evanescent modes and thereby yields superior performance.

The effect of the propagating and evanescent modes can also be seen in the character of the convergence for the three methods. The FOTC and SOTC–TE damp propagating modes well, and to the same degree. This is what gives the similar rapid initial convergence in Fig. 11a and b. The convergence of FOTC is then slowed by the solution of the evanescent portion of the spectrum. The convergence of SOTC–TE also degrades, but to a lesser degree because of the damping of the evanescent TE modes. The SOTC–OPT damps all propagating and evanescent modes to a similar degree and therefore the convergence curves of that method maintain a relatively constant rate.

Secondly, we examine the performance of the methods as the size of the sub-domains is reduced. The same physical problem, a waveguide of length $2\lambda_0/3$, is used and the mesh size is kept fixed at $h = \lambda_0/8$. The waveguide is partitioned into successively more sub-domains and solved using these three TCs. Once again, as more interfaces are introduced, more evanescent modes exist on the interfaces. Worse, the evanescent modes have less space in which to decay between interfaces and undergo multiple reflections. Because of this we see once again that the SOTC–OPT (see Fig. 12(c)), which handle all evanescent modes effectively, performs better than both the FOTC (see Fig. 12(a)) and the SOTC–TE (see Fig. 12(b)).

Lastly, we examine the behavior of the methods as the problem size increases. We use a fixed sub-domain size of $2\lambda_0/15$ and increase the length of the waveguide by increasing the number of sub-domains. The mesh size is kept fixed at $h = \lambda_0/8$. Fig. 13 demonstrates the convergence of the methods for 5, 10, 20, 50, and 100 sub-domains. In this case, the propagating modes are of great significance because the wave must travel from one end of the waveguide to the other. In this case, we see that all three methods show a dependence on the problem size. However, the FOTC (see Fig. 13(a)) and the SOTC–TE (see Fig. 13(b)) significantly outperform the SOTC–OPT because the SOTC sacrifices the convergence of propagating modes in order to account evanescent modes. No such sacrifice is made in the SOTC–TE which provides the best convergence. To consolidate this study, we increase the frequency to $f = 20$ GHz and repeat the analysis. The excitation changes to TM_{11} mode. Again, all three methods show dependences on the problem size. Fig. 14(a) shows that the convergence of FOTC degrades rapidly as the FOTC does nothing to damp evanescent modes. The SOTC–TE shows significantly improvement over FOTC, but still degrades at small residues because of the TM evanescent portion of the spectrum. From Fig. 14(c) we observe that the behavior of SOTC–OPT is similar at this higher frequency.

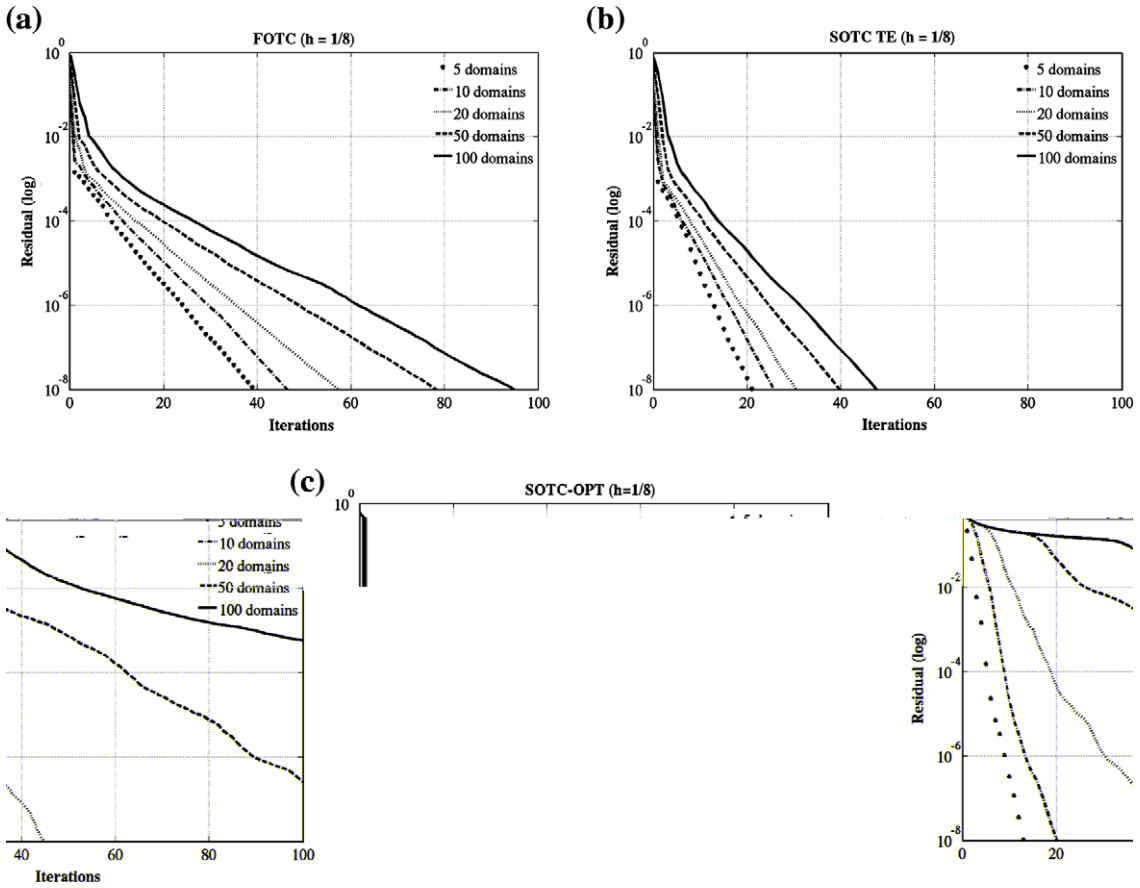

Fig. 13. Iterative solver convergence for a WR-90 waveguide with increased problem size (a) FOTC; (b) SOTC–TE; (c) SOTC–OPT.

3.3. Microstrip photonic-bandgap (PBG) structure

The last example we use is a microstrip PBG structure [21]. The geometry of the PBG structure is shown in Fig. 15. There are 10 dielectric disks between the microstrip line and the ground plane. The thickness h and width w of microstrip are 0.5 mm and 19.625 mm, respectively. The disk spacing is equal to the microstrip width and the disk radius is 3.925 mm with dielectric permittivity $\varepsilon_{\text{disk}} = 9$. The background permittivity $\varepsilon_r = 1$. We first study the convergence of our approaches with a stopping criteria of $\varepsilon = 1.0 \times 10^{-8}$ at two frequencies, $f = 3$ GHz and $f = 5$ GHz. The simulation uses 10 sub-domains with mesh size $h = \lambda_0/8$, and requires 201,735 DOFs at 3 GHz and requires 303,834 DOFs at 5 GHz. The excitation in this example is quasi-TEM. Table 3 presents the choices of parameters for SOTC–TE and SOTC–OPT at two different frequencies. Here k_- is 0 and $k_+ = \pi/w = 160.08$. The convergence histories of the iterative solvers for FOTC, SOTC–TE and SOTC–OPT are given in Fig. 16.

We see that the SOTC–TE converges much faster than the FOTC, requiring only 38 iterations while the FOTC fails to converge to $\varepsilon = 1.0 \times 1.0^{-8}$ in 100 iterations at 3 GHz. The dramatic improvement in the SOTC–TE's performance can be attributed to the small mesh elements in the vicinity of the fine features of the geometry. This leads to elements with mesh size $h \approx \lambda_0/100$ on some interfaces. The fine interface meshes give rise to evanescent modes whose eigenvalues approach the origin and deteriorate the iterative solution using the FOTC. By moving the TE evanescent eigenvalues away from the origin the SOTC–TE provides great improvement.

Next we examine the behavior of SOTC–OPT. It is worth noting that the performance of SOTC–OPT are different at $f = 3$ GHz and $f = 5$ GHz, which locate at passband at stopband, respectively. At 3 GHz, the propagating modes are of great importance because the wave travel from one end of the microstrip to the other. In this case, SOTC–OPT is even worse than FOTC. At 5 GHz, the frequency locates at the stopband. There is no wave traveling from one end to the other and the propagating modes are less important than the first case. Now the SOTC–OPT shows improvements over the FOTC. Fig. 17 shows the magnitude of the electric fields on the microstrip line at $f = 3$ GHz and $f = 5$ GHz. From Fig. 17 we can clearly see the effect of this bandgap structure.

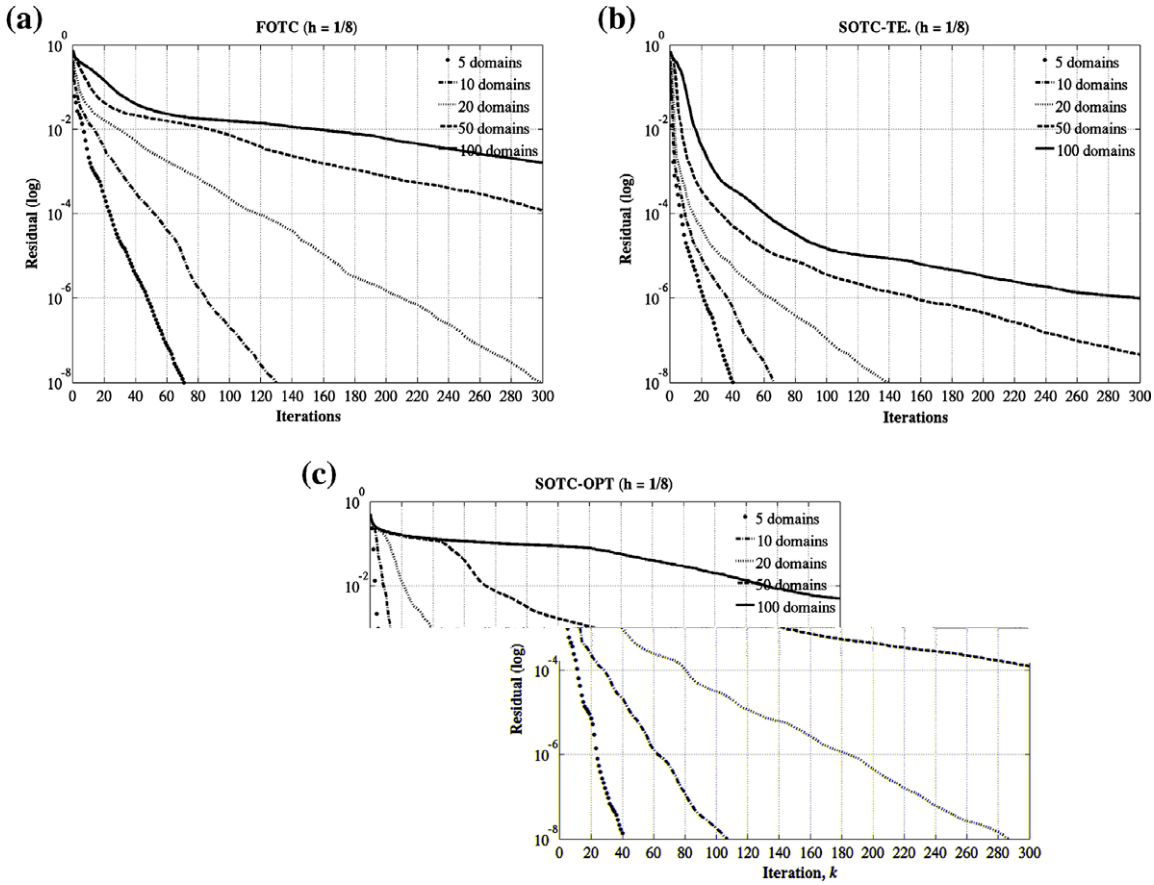

Fig. 14. Iterative solver convergence for a WR-90 waveguide with increased problem size, $f = 20$ GHz (a) FOTC; (b) SOTC–TE; (c) SOTC–OPT.

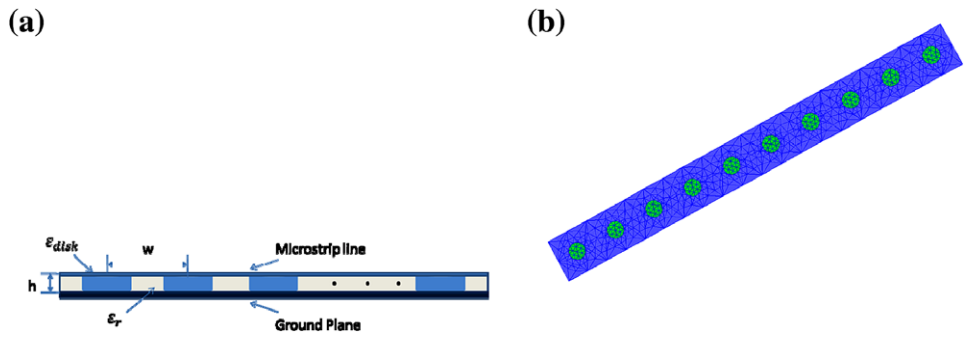

Fig. 15. Geometry of the microstrip PBG structure (a) slide view; (b) top view.

Table 3
Choices of β and p for PBG structure.

Freq.	h_{min} (m)	k_τ^{max}	β (SOTC–TE)	p (SOTC–OPT)
3GHz	0.00025	12566.4	(−7.95765e−05, 3.98159e-07)	(628.553, 628.553)
5GHz	0.00025	12566.4	(−7.95747e−05, 6.63598e-07)	(811.432, 811.432)

Lastly, the S-parameters calculated by the proposed method are compared with those from the Rayleigh multipole method [21] over a frequency band from 1.0 to 7.5 GHz in Fig. 18. In this simulation, 131 frequency points and stopping criteria $\varepsilon = 1.0 \times 10^{-3}$ are used. Good agreement is observed between the two methods.

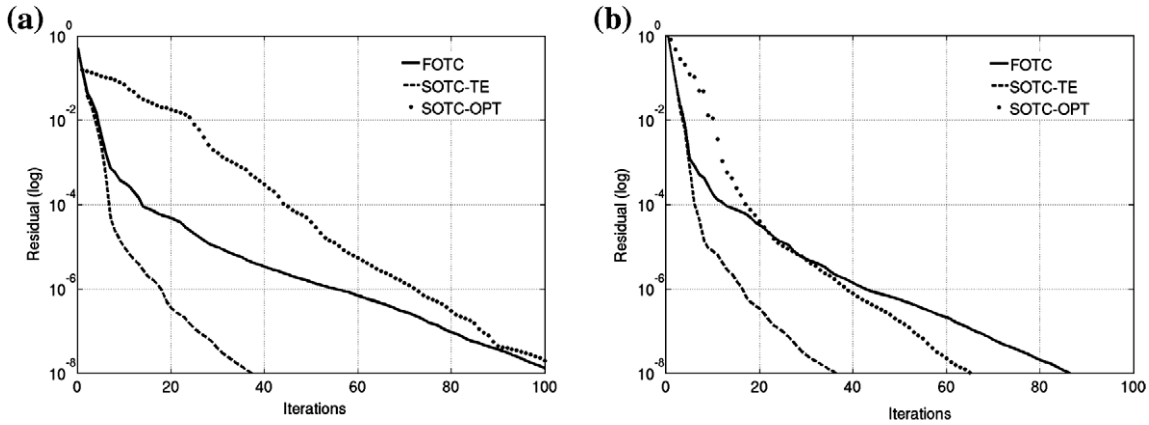

Fig. 16. Solver convergence for PBG structure (a) $f = 3$ GHz; (b) $f = 5$ GHz.

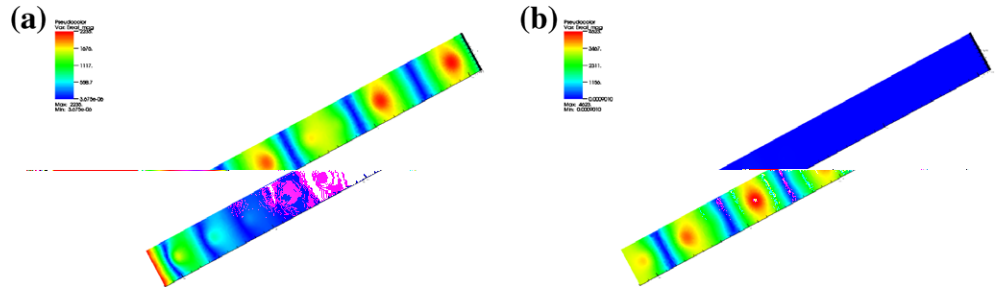

Fig. 17. The magnitude of the electric fields on the microstrip line (a) $f = 3$ GHz; (b) $f = 5$ GHz.

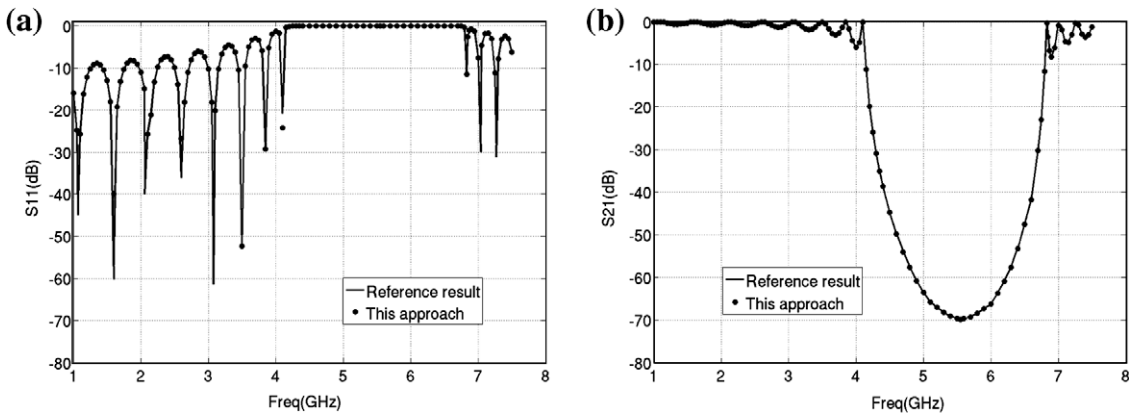

Fig. 18. The S-parameters for the PBG structure (a) S_{11} parameters; (b) S_{21} parameters.

4. Conclusion

The conventional Robin TC is effective only for propagating modes, not evanescent modes, which lead to a degradation in DD solver convergence when fine interface meshes and/or basis functions with high polynomial are used. To remedy this problem, two second order TCs were presented and shown, in agreement with the theory, to improve the convergence of the DD methods. It is clearly seen from the numerical results above that the performances of second order TCs depend to a great degree on the physics of the problem. However, the use of the SOTC–TE, unlike the SOTC–OPT, always provides superior convergence as compared to the FOTC. Although the h and sub-domain size dependencies are of some concern, in practice, we expect the SOTC–TE to perform very well.

Also, though the SOTC–TE provides significant improvement over the FOTC, it was shown theoretically and experimentally that is fails to address the convergence of TM evanescent modes. While it was also demonstrated that these eigenvalues do not approach the origin and thereby degrade iterative solution performance as rapidly as the TE evanescent modes, these modes do impact solver convergence. It is therefore desirable to have a full SOTC that accounts for both TE and TM evanescent modes. We may address this issue in the future work. Moreover, a coarse space correction/global preconditioner may be very beneficial in reducing the number of iterations, particularly for the transport-dominated problems. We shall report in the future our efforts in coarse space correction schemes. To this end, although these TCs are derived and tested in planar surfaces, we have also applied them to examples with non-planar surfaces without noticeable differences.

References

[1] P. Monk, Finite Element Methods for Maxwell's Equations. Numerical Mathematics and Scientific Computation, Oxford University Press, New York, 2003.
[2] B.-F. Smith, P. Bjørstad, W. Gropp, Domain Decomposition Parallel Multilevel Methods for Elliptic Partial Differential Equation, Cambridge University Press, New York, 1996.
[3] A. Quarteroni, A. Valli, Domain Decomposition Methods for Partial Differential Equations, Oxford University Press, New York, 1999.
[4] A. Toselli, O. Widlund, Domain Decomposition Methods-Algorithms and Theory, Springer, Berlin, 2005.
[5] B. Després, Méthodes de décomposition de domaine pour les problèmes de propagation d'ondes en régime harmonique. Ph.D. Thesis, Université Dauphine, Paris IX, 1991.
[6] J.-D. Benamou, B. Després, A domain decomposition method for the Helmholtz equation and related optimal control problems, J. Comput. Phys. 136 (1997) 68–82.
[7] B. Stupfel, A fast domain decomposition method for the solution of electromagnetic scattering by large objects, IEEE Trans. Antennas Propagat. 44 (10) (1996) 1375–1385.
[8] C.T. Wolfe, U. Navsariwala, S.D. Gedney, A parallel finite-element tearing and interconnecting algorithm for solution of the vector wave equation with PML absorbing medium, IEEE Trans. Antennas Propagat. 48 (2) (2000) 278–284.
[9] B. Stupfel, M. Mognot, A domain decomposition method for the vector wave equation, IEEE Trans. Antennas Propagat. 48 (5) (2000) 653–660.
[10] S.-C. Lee, M. Vouvakis, J.F. Lee, A non-overlapping domain decomposition method with non-matching grids for modeling large finite antenna arrays, J. Comput. Phys. 203 (1) (2005) 1–21.
[11] M.N. Vouvakis, Z. Cendes, J.-F. Lee, A FEM domain decomposition method for photonic and electromagnetic band gap structures, IEEE Trans. Antennas Propagat. 54 (2) (2006) 721–733.
[12] Y.-J. Li, J.-M. Jin, A new dual-primal domain decomposition approach for finite element simulation of 3-D large-scale electromagnetic problems, IEEE Trans. Antennas Propagat. 55 (10) (2007) 2803–2810. Oct..
[13] K. Zhao, V. Rawat, S.-C. Lee, J.-F. Lee, A domain decomposition method with nonconformal meshes for finite periodic and semi-periodic structures, IEEE Trans. Antennas Propagat. 55 (9) (2007) 2559–2570.
[14] F. Gündes, Higher order absorbing boundary conditions for vector finite element method. Master's Thesis, The Ohio State University, 2006.
[15] P. Collino, G. Delbue, P. Joly, A. Piacentini, A new interface condition in the onoverlapping domain decomposition for the Maxwell's equation, Comput. Meth. Appl. Meth. Eng. 148 (1997) 195–207.
[16] M.J. Gander, F. Magoulès, F. Nataf, Optimized Schwarz methods without overlap for the Helmholtz equations, SIAM J. Sci. Comput. 24 (1) (2002) 38–60.
[17] A. Alonso-Rodriguez, L. Gerardo-Giorda, New non-overlapping domain decomposition methods for the harmonic Maxwell system, SIAM J. Sci. Comput. 28 (1) (2006) 102–122.
[18] V. Dolean, M.J. Gander, L. Gerardo-Giorda, Optimized Schwarz methods for Maxwell's equations, SIAM J. Sci. Comput. 31 (3) (2009) 2193–2213.
[19] J.-F. Lee, D.-K. Sun, p-Type multiplicative Schwarz (pMUS) method with vector finite elements for modeling three-dimensional waveguide discondinuities, IEEE Trans. Microwave Theory Tech. 52 (2004) 864–870.
[20] D.-K. Sun, J.-F. Lee, Z. Cendes, Construction of nearly orthogonal Nedelec bases for rapid convergence with multilevel preconditioned solvers, SIAM J. Sci. Comput. 23 (4) (2001) 1053–1076.
[21] D.-E. Schaub, D.-R. Oliver, Rapid simulation of linear PBG Microstrip structures using the Rayleigh multipole method, IEEE Trans. Microwave Theory Tech. 56 (2006) 49–55.
[22] V. Rawat, Finite element domain decomposition with second order transmission condition for time harmonic electromagnetic problem, Ph.D. Thesis, The Ohio State University, 2009.